Chinese Chemical Letters 37 (2026) 111192

Contents lists available at ScienceDirect

Chinese Chemical Letters

journal homepage: www.elsevier.com/locate/cclet

Fabrication of three-dimensional porous β-PbO_2@Ti mesh anode for enhanced electrocatalytic ozone production

Mengqing Hu[a,1], Di Zhao[a,1], Yun Wang[a], Jian Kang[a,b], Ming Zhou[a], Huai Qin Fu[a], Bernt Johannessen[c], Joshua Harbort[d], Jeffrey Harmer[d], Xinlong Yan[e], Yajie Shu[f], Porun Liu[a,*], Huajie Yin[b,*], Huijun Zhao[a,*]

[a] School of Environment and Science, Gold Coast Campus, Griffith University, Gold Coast, QLD 4222, Australia
[b] Centre for Environmental and Energy Nanomaterials, Institute of Solid State Physics, HFIPS, Chinese Academy of Sciences, Hefei 230031, China
[c] Australian Synchrotron, ANSTO, Clayton, VIC 3168, Australia
[d] Centre for Advanced Imaging, St Lucia Campus, University of Queensland, Brisbane, QLD 4072, Australia
[e] Jiangsu Province Engineering Research Center of Fine Utilization of Carbon Resources, School of Chemical Engineering & Technology, China University of Mining and Technology, Xuzhou 221116, China
[f] National Joint Laboratory for Advanced Textile Processing and Clean Production, Wuhan Textile University, Wuhan 430200, China

ARTICLE INFO

Article history:
Received 20 January 2025
Revised 31 March 2025
Accepted 9 April 2025
Available online 9 April 2025

Keywords:
Three-dimensional porous anode
β-PbO_2
Electrochemical ozone production (EOP)
Structural regulation
Oxygen vacancy

ABSTRACT

Electrochemical ozone production (EOP) has emerged as an eco-friendly, cost-effective alternative to the current industrial corona discharge approach; however, the low Faradaic efficiency (FE) of electrochemical ozone production (EOP) and anode instability at high current density of the conventional plate electrode hinders its actual application. Herein, we introduce a strategy to enhance the EOP performance of β-PbO_2 by constructing a three-dimensional (3D) porous architecture. This approach elevates the EOP FE of the 3D-porous β-PbO_2@Ti mesh anode (14.73 %) to over twice that of the conventional β-PbO_2@Ti mesh (6.11 %) at a current density of 100 mA/cm^2. Furthermore, it demonstrates a robust service life and consistent O_3 production capability, sustaining stable output over extended periods (70 h, 20 h) at higher current densities (100, 250 mA/cm^2). This strategy of external structural anode modification exerts a beneficial effect on the internal oxygen environment within β-PbO_2, increasing the availability of adsorption sites for oxygen intermediates and thus providing favorable conditions for efficient O_3 generation. This work shows the potential of 3D porous anode for practical industrial deployment of EOP.

© 2026 Published by Elsevier B.V. on behalf of Chinese Chemical Society and Institute of Materia Medica, Chinese Academy of Medical Sciences.

Ozone (O_3) is recognized as a potent green oxidant, rendering it exceptionally effective in the realms of environmental conservation and industrial production [1,2]. Conventionally, O_3 is produced *via* corona discharge technology which is encumbered by high energy demands (a few thousand volts) and the complexity of the requisite apparatus (air drying device and cooling system) [3,4]. In recent years, the electrolytic oxidation of water at appropriate anodic materials for the generation of O_3 has emerged as a promising alternative, attributed to its environmentally friendly, operationally straightforward, and easily regulatable nature [5–7]. Nevertheless, as delineated in the subsequent reaction equations for water oxidations (Eqs. 1 and 2), the potential for oxygen evolution reaction (OER) is lower than that for electrochemical O_3 production (EOP), rendering oxygen an inevitable primary competing by-product [8]. Consequently, to ameliorate the selectivity towards O_3 production, it is necessary to suppress the evolution of oxygen.

$$2H_2O \rightarrow O_2 + 4H^+ + 4e^-,\ E_0 = 1.23\ V \quad (1)$$

$$3H_2O \rightarrow O_3 + 6H^+ + 6e^-,\ E_0 = 1.51\ V \quad (2)$$

Anodic materials significantly influence the efficiency and purity of O_3 generation. To ensure predominant generation of O_3 instead of O_2, it is essential to tailor the anode materials with a high OER overpotential. Anodes made of platinum (Pt) [9,10], or boron-doped diamond (BDD) [11,12] characterized by a high OER overpotential are employed as anodic materials in O_3 generation due to their excellent O_3 selectivity and chemical robustness [12]. However, prohibitive costs preclude them from being the prime choice for commercial-scale production. Lead dioxide (β-PbO_2), notable for cost-effectiveness, catalytic efficiency and long-term

* Corresponding authors.
E-mail addresses: p.liu@griffith.edu.au (P. Liu), yinhj@issp.ac.cn (H. Yin), h.zhao@griffith.edu.au (H. Zhao).
[1] These authors contributed equally to this work.

https://doi.org/10.1016/j.cclet.2025.111192
1001-8417/© 2026 Published by Elsevier B.V. on behalf of Chinese Chemical Society and Institute of Materia Medica, Chinese Academy of Medical Sciences.

durability, has emerged as exemplary anode materials, which effectively promote the oxidation of water to O_3 [13,14]. Despite advancements in β-PbO_2 anode for O_3 production, challenges such as limited selectivity and low current density persist, affecting the purity and yield of O_3 [15]. The three-dimensional (3D) porous structure modification strategy is anticipated to address the aforementioned issues associated with β-PbO_2 anode [16–18]. The primary advantage of this enhancing strategy lies in the increased specific surface area of the β-PbO_2 anode, offering abundant active sites for electrochemical reactions and enhancing electrolyte transport and diffusion, thereby significantly boosting the production efficiency [14,17,19]. Based on the aforementioned merits, it is posited that 3D porous β-PbO_2 anodes hold considerable potential for enhancing O_3 generation.

To achieve the targeted functionality, a hard-template-assisted fabrication approach is proposed. Silica (SiO_2) sphere is an inorganic non-metallic material with substantial hardness and chemically inert properties [20], which can self-assemble into ordered structures, serving as sacrificial templates to guide the crystallization of β-PbO_2 [21]. Upon removal of the SiO_2 template, a nanoscale-structured 3D porous β-PbO_2 anode is obtained. This templated synthesis method allows for precise tuning of the pore architecture, which enhances the density of β-PbO_2 active sites and increases accessible surface area, thereby facilitating electrolyte diffusion and improving the anode electrochemical reactivity. Moreover, titanium (Ti) substrate is prevalently utilized in various high-potential electrochemical reaction systems, attributed to their excellent electrical conductivity, chemical stability, and mechanical integrity [22]. Notably, in comparison to Ti foils, Ti meshes with excellent void structure and high specific surface areas may serve as superior substrates for the *in-situ* robust integration of porous β-PbO_2 [23–25]. These aspects collectively forge advantageous conditions for the electrochemical generation of O_3.

In this study, a 3D porous β-PbO_2 anode (3D-porous β-PbO_2) was successfully fabricated *in situ* on the Ti mesh substrate through an anodic deposition strategy employing SiO_2 sphere template. After template removal, the 3D-porous β-PbO_2 anode demonstrates enhanced current density and improved selectivity for electrochemical O_3 generation. The superior performance in O_3 production, compared to conventional β-PbO_2 anode, can be ascribed to the development of a 3D porous architecture, which offers an increased number of active sites for electrocatalytic reactions, and optimizing the Pb-O coordination environment to increase oxygen vacancies. Furthermore, this porous β-PbO_2 anode exhibits commendable catalytic stability and corrosion resistance, maintaining consistent electrochemical performance over sustained periods under high potential and strongly acidic conditions. The demonstrated material engineering strategy employed for β-PbO_2 anode is expected to provide more efficient and cost-effective solutions in EOP technologies.

The fabrication process of the 3D-porous β-PbO_2 anode is shown in Figs. 1a and b. The SiO_2 sphere structural template was self-assembled on a Ti mesh (Fig. S1 in Supporting information), followed by the growth of a β-PbO_2 layer employing a one-step anodic deposition technique. Subsequently, the template was dissolved using potassium hydroxide, culminating in the acquisition of a 3D-porous β-PbO_2@Ti mesh anode. As delineated in Fig. S2 (Supporting information), the Ti mesh substrate exhibits a uniform network architecture, providing abundant sites for catalyst growth. Further microscopic examination revealed a roughened surface, which increases the amount of active material grown on it and stabilizes active entities to prevent detachment during electrochemical reactions. Concurrently, β-PbO_2 featuring a 3D-porous configuration was synthesized on a Ti mesh through template-assisted electrodeposition, poised to further enhance the electrocatalytic performance of the anode. The morphology of the SiO_2 as

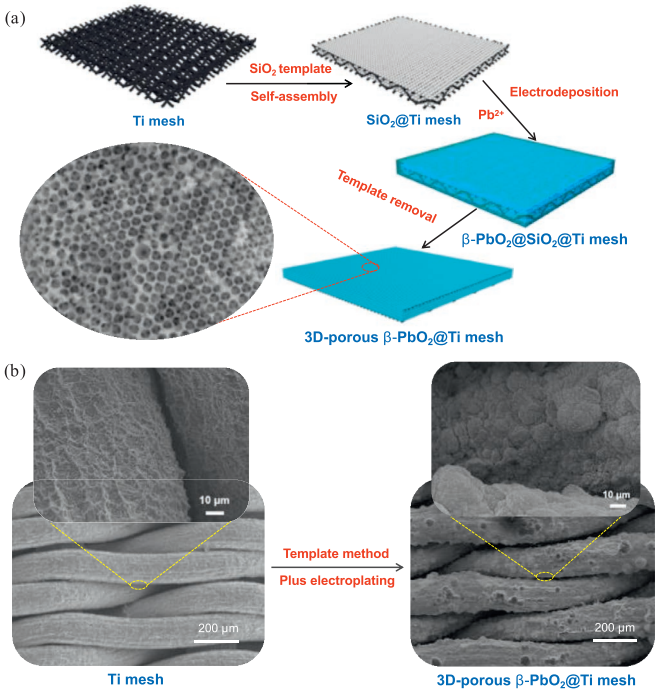


Fig. 1. (a) Schematic diagram of the fabrication process and (b) the corresponding SEM images of the Ti mesh and 3D-porous β-PbO_2@Ti mesh anodes.

a template, as shown in Fig. S3 (Supporting information), reveals uniformly spherical shape with a smooth surface with an approximate diameter of 200 nm. An orderly self-assembly of the SiO_2 spheres results to uniform distribution of the voids on the Ti mesh where the subsequent filling of β-PbO_2 was electrochemically deposited. β-PbO_2@Ti mesh was fabricated without the presence of SiO_2 spheres for comparison purpose.

To elucidate the composition and structure of the synthesized anodes, comprehensive analyses employing X-ray diffraction (XRD), and Raman spectroscopy were conducted. The XRD patterns of both 3D-porous β-PbO_2@Ti mesh and β-PbO_2@Ti mesh are depicted in Fig. 2a, revealing pronounced diffraction peaks at 2θ angles of 25.4°, 31.9°, 36.8°, and 49.1°, corresponding to the (110), (101), (111), and (211) crystallographic planes of the β-PbO_2 phase (PDF#41-1492), respectively [26]. This observation unequivocally verifies the successful synthesis of the β-PbO_2 crystal phase, which is consistent with the high-resolution transmission electron microscopy (HRTEM) results. Raman spectroscopic analysis further delineates the crystal structure characteristics (Fig. S4 in Supporting information), and 3D-porous β-PbO_2@Ti mesh anode displays peaks approximately at 515 cm^{-1}, indicative of vibrations pertaining to the Pb-O bonds within the tetragonal β-PbO_2 crystal lattice [27,28]. However, acquiring distinct Raman signals for tetragonal lead oxide proves challenging, because the β-PbO_2 tends to decompose into other lead oxide compounds under the laser irradiation used in Raman microscope, even at exceedingly low laser power settings [27]. Consequently, the β-PbO_2 phase manifests as a subdued peak, while the decomposition products exhibit pronounced peaks at 165 and 228 cm^{-1}, characteristic of the scrutinyite (α-PbO_2) phase [28]. Importantly, the intensity of the decomposition product peaks in the 3D-porous β-PbO_2@Ti mesh is markedly lower than in ordinary β-PbO_2@Ti mesh, suggesting enhanced endurance of the porous β-PbO_2 structure.

Subsequently, morphology of the 3D-porous β-PbO_2@Ti mesh anode was observed by SEM. Fig. S5 (Supporting information) distinctly illustrates that the β-PbO_2 layer uniformly covers the surface of the porous Ti mesh, displaying an overall surface com-

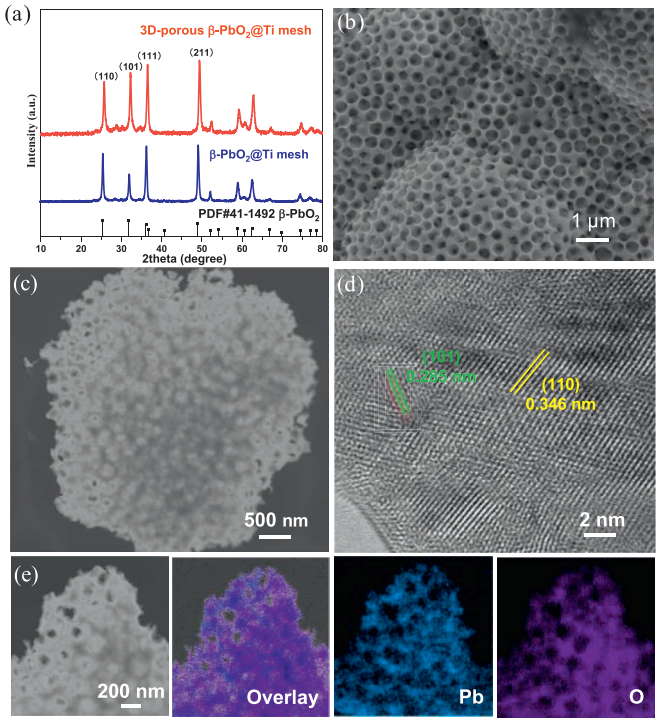


Fig. 2. (a) XRD patterns of 3D-porous β-PbO_2@Ti mesh and β-PbO_2@Ti mesh. (b) SEM, (c) TEM and (d) HRTEM images, (e) STEM image and corresponding element mappings of 3D-porous β-PbO_2@Ti mesh.

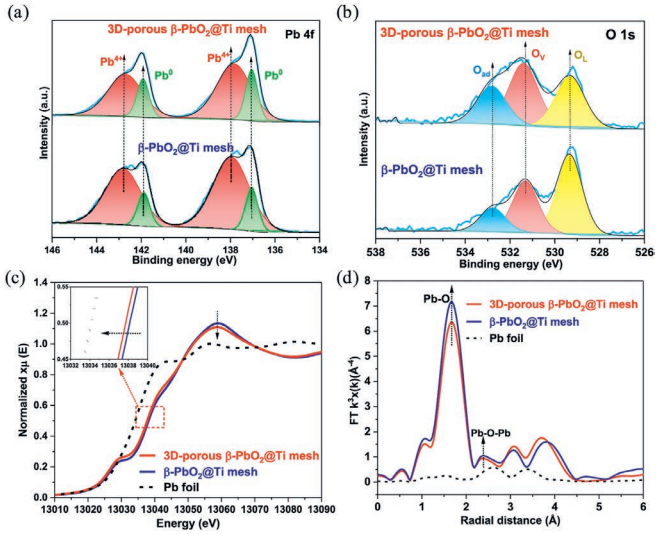


Fig. 3. (a) Pb 4f and (b) O 1s XPS spectra, Pb L_3-edge (c) XANES and (d) FT-EXAFS spectra of as-prepared 3D-porous β-PbO_2@Ti mesh.

posed of closely connected, unevenly sized spherical protrusions. The SEM image at higher magnification reveals that the β-PbO_2 layer successfully exhibit a porous structure, with pore sizes primarily distributed around 200 nm and uniformly dispersed, indicating the precise control over the pore structure (Fig. 2b). Through TEM analysis, a deeper understanding of the microstructure of 3D-porous β-PbO_2 was achieved, showing a highly porous 3D network structure and a rough surface (Fig. 2c). Notably, the exposure of crystal facets is crucial for electrochemical activity and stability. Clear lattice fringes observed in HRTEM images, with precise measurements of lattice spacings of 0.346 nm and 0.285 nm, confirm that the tetragonal β-PbO_2 crystals are mainly dominated with (101) and (110) facets, respectively (Fig. 2d). The EDS mapping analysis demonstrates that Pb and O elements are uniformly distributed throughout the entire porous β-PbO_2 layer without any noticeable aggregation or segregation (Fig. 2e). This uniformity suggests that the growth of 3D-porous β-PbO_2 during the electrochemical deposition process is uniform, which contributes to the enhanced mass transport, charge transfer efficiency and overall catalytic performance. In stark contrast to 3D-porous β-PbO_2, the morphology of β-PbO_2 illustrates a bulky structure growth on the Ti mesh (Fig. S6 in Supporting information). These variably sized block crystals densely stack together to form the compact β-PbO_2 layer. Through the analysis above, we reasonably conjecture that the unique 3D-porous β-PbO_2@Ti mesh anode offers a superior advantage in electrochemical catalysis over block β-PbO_2@Ti mesh. This can be attributed to 3D porous morphology, which is conducive to the permeation and diffusion of electrolytes, enriched surface reaction sites, and rapid charge transfer, enhancing the catalytic activity and robustness of the anode.

To investigate the elemental composition and electronic structure of the anode material, X-ray photoelectron spectroscopy (XPS) was performed. The XPS survey spectra of the fabricated β-PbO_2 anodes reveal peaks attributed to Pb and O (Fig. S7 in Supporting information), aligning with the EDS result and reaffirming the successful synthesis of PbO_2. A noteworthy observation is the elevated oxygen content in 3D-porous β-PbO_2@Ti mesh compared to β-PbO_2@Ti mesh. This increase in oxygen content could potentially augment the surface activity of the material, facilitating the adsorption of H_2O molecules [29]. The high-resolution XPS spectra for the Pb 4f region, depicted in Fig. 3a, show peaks at 142.8 eV and 137.9 eV, ascribed to the Pb^{4+}, and peaks at 141.9 and 137.1 eV, corresponding to Pb^0 [30]. Compared with compact β-PbO_2@Ti mesh, the 3D-porous β-PbO_2@Ti mesh shows a lower Pb^{4+}, which is often associated with the formation of oxygen vacancies that serve as active sites, facilitating water molecule adsorption and activation [31]. Furthermore, the O 1s analysis reveals two distinct peaks at 529.2, 531.3, and 532.7 eV, corresponding to strongly bound lattice oxygen (Pb-O), oxygen vacancy (O_V) and surface-adsorbed oxygen (O–H group), respectively (Fig. 3b) [32,33]. Notably, an increase in O_v and surface-adsorbed oxygen in 3D-porous β-PbO_2 is observed, which is conducive to the provision of additional adsorption sites for oxygen species, thereby potentially facilitating enhanced catalytic activity. Moreover, as shown in Fig. S8 (Supporting information), the EPR test detected a distinct signal at $g = 2.08$, with 3D-porous β-PbO_2 exhibiting an enhanced intensity, confirming the increased O_v. To further elucidate the electronic valence state and coordination environment of Pb, X-ray absorption spectroscopy (XAS) was conducted at the Pb L_3-edge. The X-ray absorption near-edge structure (XANES) spectrum (Fig. 3c) reveals that the absorption edge energy of the 3D-porous β-PbO_2 is shifted negatively compared to compact β-PbO_2, with a weaker white line peak intensity. This indicates a reduction in the high-valence Pb^{4+} of 3D-porous β-PbO_2, leading to the formation of lower-valence Pb. This reduction may cause the release of oxygen ions, thereby increasing the number of oxygen vacancies [34]. Fourier transform extended X-ray absorption fine structure (FT-EXAFS), and K-space fitted EXAFS spectra (Fig. 3d and Fig. S9 in Supporting information) show that the primary peak at 1.7 Å corresponds to the Pb-O scattering interaction and the 3D-porous β-PbO_2 displays a slightly weaker peak, indicating a reduced Pb-O coordination. The lower coordination number of Pb-O suggests the removal of oxygen atoms from the crystal lattice, leading to an increase in oxygen vacancies [34]. This 3D porous surface modification effectively optimizes the internal atomic arrangement of β-PbO_2, thereby enhancing EOP efficiency.

The electrocatalytic activity of β-PbO_2 anodes for O_3 gas generation was investigated by employing a three-electrode con-

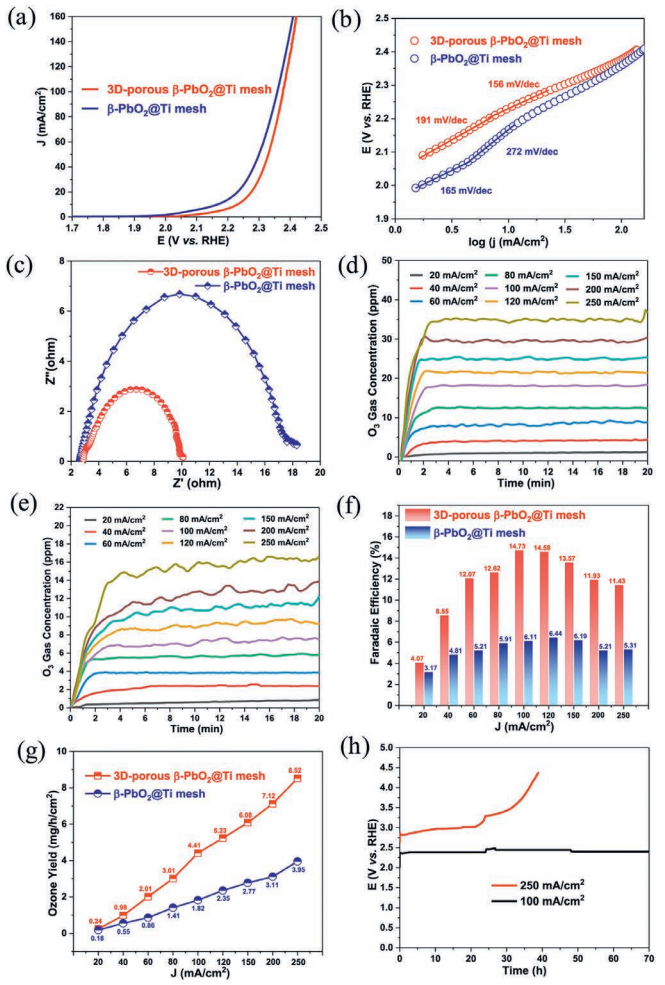


Fig. 4. (a) LSV curves, (b) Tafel plots, (c) Nyquist plots of the electrochemical impedance spectra (EIS) of 3D-porous β-PbO_2@Ti mesh and β-PbO_2@Ti mesh. The dynamic concentration of O_3 gas on (d) 3D-porous β-PbO_2@Ti mesh and (e) β-PbO_2@Ti mesh. (f) Faradaic efficiencies and (g) O_3 gas yield with various current densities. (h) Stability of 3D-porous β-PbO_2@Ti mesh on constant current densities of 100 mA/cm^2 and 250 mA/cm^2.

figuration in a 0.5 mol/L H_2SO_4 medium at room temperature. Fig. 4a illustrates the linear sweep voltammetry (LSV) polarization curves for both anodes. 3D-porous β-PbO_2@Ti mesh manifests higher potential (2.23 V *vs.* RHE) at a current density of 10 mA/cm^2, whereas the ordinary β-PbO_2@Ti mesh is merely 2.16 V *vs.* RHE. The larger overpotential serves to suppress oxygen liberation from competing reactions, suggesting its great potential for targeted O_3 gas production. Moreover, the Tafel plot of the anodic catalytic reaction is featured with two distinct slopes (Fig. 4b). At lower current densities, the predominance of the OER reaction is posited, with negligible EOP activity. The Tafel slope of the 3D-porous β-PbO_2@Ti mesh anode is larger, indicating its diminished OER activity. Potentially, this anode is beneficial to the EOP catalytic reaction. Conversely, at high current densities where EOP markedly contributes to the reaction, the 3D-porous β-PbO_2@Ti mesh anode exhibits a reduced Tafel slope, indicative of augmented catalytic activity, possibly contributed by an enhanced EOP selectivity. Moreover, the electrochemical double layer capacitance (C_{dl}) reflects the charge storage capacity of the anode interface, intrinsically related to the surface area of the anode, thereby serving as a metric for assessing the electrochemically active surface area (ECSA) of the anode [35]. C_{dl} values are extracted from cyclic voltammograms (CV) measured with varying scan rates (5, 10, 20, 40, 60, 80 and 100 mV/s). Figs. S10 and S11 (Supporting information) display the CV curves for 3D-porous β-PbO_2@Ti mesh and β-PbO_2@Ti mesh across diverse scanning rates within the potential of 1.69–1.79 V *vs.* RHE. Notably, as shown in Fig. S12 (Supporting information), the 3D-porous β-PbO_2@Ti mesh attains a larger C_{dl} of approximately 4.6 mF/cm^2, evidencing a substantial electrochemical specific surface area conducive to exposing more active sites and thus elevating the electrocatalytic activity. Additionally, electrochemical impedance spectroscopy (EIS) is used to evaluate the charge transfer resistance (R_{ct}) of the anode to reflect the electrochemical performance of the material [36]. Nyquist plots delineate the impedance characteristics of disparate β-PbO_2 anodes. Relative to the β-PbO_2@Ti mesh (14 Ω), the 3D-porous variant exhibits a smaller R_{ct} (6 Ω) (Fig. 4c), denoting lower charge transfer impedance and, thus, a more efficacious EOP reaction kinetics.

Subsequently, the generation of O_3 gas was assessed both qualitatively and quantitatively. The gaseous output from the anode, under a current density of 100 mA/cm^2 for a duration of 2 min, induced a color transition in the wet starch potassium iodide (SSKI oral solution) test paper to dark blue (Fig. S13 in Supporting information), unequivocally evidencing O_3 production. Moreover, the potassium iodide (SSKI oral solution) test strip treated with 3D-porous β-PbO_2@Ti mesh exhibits a more intense darkening, indicative of a higher yield of O_3 gas. As shown in Figs. 4d and e, a progressive increment in current density causes a concomitant rise in the steady concentration of O_3 gas and the corresponding applied voltages (Figs. S14 and S15 in Supporting information). Notably, the O_3 gas steady concentration associated with 3D-porous β-PbO_2@Ti mesh anode consistently surpasses that of β-PbO_2@Ti mesh. At a current density of 250 mA/cm^2, the steady concentration of O_3 gas by 3D-porous β-PbO_2@Ti mesh reaches up to 35 ppm, markedly exceeding that of the β-PbO_2@Ti mesh (16 ppm). For both anodes, with the increase in current density, the Faradaic efficiency (FE) related to O_3 generation gradually increases and subsequently declines with a further increase in current density due to the competitive OER. At a current density of 100 mA/cm^2, 3D-porous β-PbO_2@Ti mesh achieves a peak FE of 14.73 %, significantly outperforming the β-PbO_2@Ti mesh, which records merely 6.11 % (Fig. 4f). Correspondingly, the O_3 yield for 3D-porous β-PbO_2@Ti mesh reach 8.53 mg/h/cm^2 at a current density of 250 mA/cm^2, substantially surpassing the output from β-PbO_2@Ti mesh (3.95 mg/h/cm^2) (Fig. 4g), underscoring the enhanced catalytic efficacy of the porous anode material in O_3 production. Compared with other reported β-PbO_2 anodes, the fabricated 3D-porous β-PbO_2@Ti mesh manifests a higher EOP FE at a lower potential (Table S1 in Supporting information). Furthermore, the durability of anode materials is paramount for the practical deployment of electrocatalytic processes. The robustness of 3D-porous β-PbO_2@Ti mesh was scrutinised across varying current densities, sustaining consistent and stable EOP performance for in excess of 70 h at a current density of 100 mA/cm^2 (Fig. 4h). The composition and morphology of the after-reaction anode were tested, displaying negligible alterations in the 3D-porous β-PbO_2@Ti mesh, with the morphology integrity of the 3D-porous β-PbO_2 layer remaining unscathed, without obvious shedding (Fig. S16 in Supporting information). Even under the stringent conditions of a high current density of 250 mA/cm^2, the 3D-porous β-PbO_2@Ti mesh anode retains its catalytic property for over 20 h (Fig. 4h), with subsequent deactivation attributed to the detachment of the catalytic layer. This phenomenon is corroborated in the SEM images (Fig. S17 in Supporting information). Also, the emergence of the Ti substrate peaks on the XRD result further confirms the shedding of the 3D-porous β-PbO_2 catalytic layer (Fig. S18 in Supporting information). Moreover, O_3 production during electrocatalytic water decomposition by 3D-porous β-PbO_2@Ti mesh anode occurs at high potentials. To rule out the possibility of self-oxidation to ozone at these potentials, we used commercial RuO_2, a benchmark OER cat-

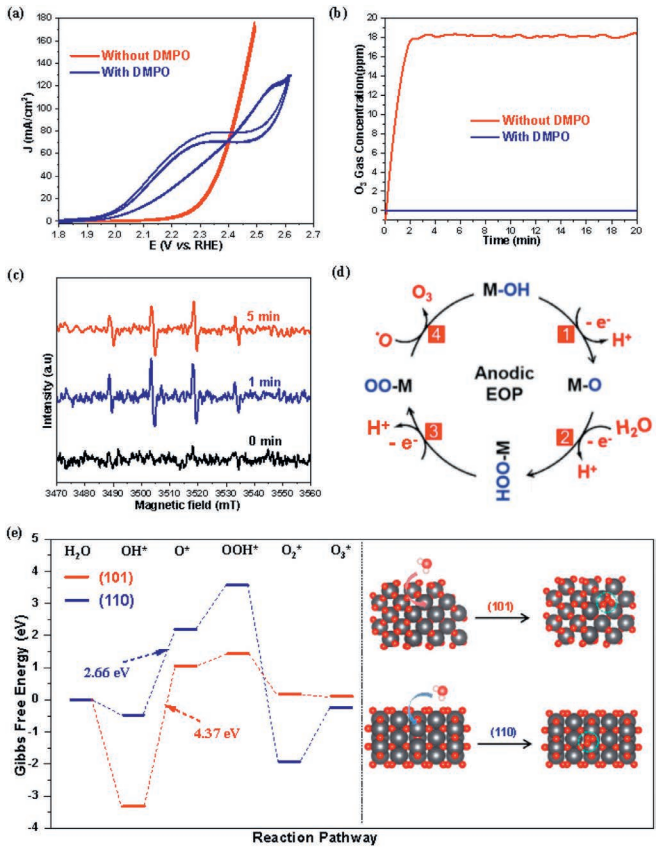


Fig. 5. (a) CV curves and (b) gaseous O_3 dynamic concentrations at a constant current density of 100 mA/cm^2 of 3D-porous β-PbO_2@Ti mesh anode with and without DMPO. (c) DMPO spin-trapping EPR spectra of the electrolyte collected after the EOP at a constant current density of 20 mA/cm^2 after varied duration. (d) Proposed anodic EOP mechanisms on the 3D-porous β-PbO_2@Ti mesh anode. (e) Potential free energy diagrams for O_3 generation on PbO_2 (101) and (110) surfaces with O_V. Black and red spheres represent Pb and O, respectively.

alyst, for qualitative and quantitative O_3 tests across a potential range of 2.0–2.6 V *vs.* RHE. As shown in Figs. S19 and S20 (Supporting information), starch potassium iodide (SSKI oral solution) exhibited minimal color change to blue, and real-time quantification confirmed negligible O_3 production. In addition, the 3D-porous β-PbO_2@Ti mesh anode was thoroughly oxidized prior to the EOP. These findings confirm that ozone generation at high potentials is driven by the catalytic action of 3D-porous β-PbO_2@Ti mesh rather than self-oxidation. The aforementioned results verify that the 3D-porous β-PbO_2@Ti mesh anode exhibits an outstanding O_3 gas generation rate and sustains stable output over extended periods at elevated current densities, positioning it as a promising EOP anode material with significant potential for application.

To explore the mechanism of EOP on 3D-porous β-PbO_2@Ti mesh anode, 5,5-dimethyl-1-pyrrolidine-oxide (DMPO) was employed as a spin trapping agent for the active intermediates. The CV curves, as illustrated in Fig. 5a, reveal significant alterations after DMPO addition, notably a substantial decrease in onset potential and current density. Concurrently, at equivalent current densities, the stable production concentration of O_3 markedly declined, culminating in negligible O_3 gas formation (Fig. 5b). These phenomena are attributed to the fact that DMPO scavenged hydroxyl radicals (·OH), a pivotal intermediate in the O_3 generation pathway. This hypothesis is further substantiated by electron paramagnetic resonance (EPR) spectroscopy results. As shown in Fig. 5c, no EPR signal is detected before initiating the reaction. In stark contrast, a characteristic quadruplet signal with a peak height ratio of 1:2:2:1 emerges in the EPR spectrum of the reaction medium collected after the EOP reaction for 1 min, indicative of the presence of DMPO–OH adduct [37,38]. This signature is similarly observed for the reaction medium collected in 5 min, confirming the generation of ·OH radicals in the EOP reaction. Drawing from these observations and reported literature, the mechanism of O_3 generation on the 3D-porous β-PbO_2@Ti mesh is proposed to involve the following processes (Fig. 5d) [39–42]:

$$H_2O(ads) \rightarrow \cdot OH(ads) + H^+ + e^- \quad (3)$$

$$OH(ads) \rightarrow \cdot O(ads) + H^+ + e^- \quad (4)$$

$$O(ads) + H_2O(ads) \rightarrow \cdot OOH(ads) + H^+ + e^- \quad (5)$$

$$OOH(ads) \rightarrow \cdot O_2(ads) + H^+ + e^- \quad (6)$$

$$O_2(ads) + \cdot O(ads) \rightarrow O_3(ads) \rightarrow O_3(g) \quad (7)$$

To further elucidate the intrinsic mechanisms underlying the enhanced EOP activity, density functional theory (DFT) calculations were conducted to explore the lattice oxygen oxidation (LOM) pathway of the EOP reaction on a 3D-porous β-PbO_2 catalyst. Gibbs free energy changes (ΔG) for each of the five reaction steps in the EOP process were calculated using the hydrogen electrode method [43], with the step exhibiting the highest ΔG identified as the rate-determining step (RDS) of the EOP reaction. The EOP activity of the 3D-porous β-PbO_2 is primarily governed by the ΔG of the RDS, with lower ΔG values correlating with higher surface EOP activity. As illustrated in Figs. S21 and S22 (Supporting information), the formation of O_3 on the surface is likely a coupled reaction involving both O_2* and O* species. Initially, water dissociates to produce OH*, which subsequently reacts with OH^-, forming an O*. This O* species then adsorbs and interacts with OH^- to yield an OOH* intermediate. Subsequently, the OOH* further reacts with additional OH^-, producing O_2* that adsorbs onto the surface. Finally, the adsorbed O_2* reacts with neighboring O* species to form O_3* on the surface. As shown in Fig. 5e, for the (101) crystal facet of 3D-porous β-PbO_2, the step with the highest ΔG is $OH^* \rightarrow O^* + H^+ + e^-$, with an energy difference of 4.37 eV. A similar computational analysis was performed for the (110) crystal plane, revealing $OH^* \rightarrow O^* + H^+ + e^-$ step has a highest ΔG of 2.66 eV. Notably, the (110) surface of β-PbO_2 demonstrates a lower ΔG for the RDS (Table S2 in Supporting information). This suggests that the reaction pathway on the (110) crystal surface is more conducive to oxygen migration and O_3 generation compared to the (101) counterpart. Moreover, the aforementioned results show that 3D-porous β-PbO_2 increases the density of O_V compared to traditional β-PbO_2. O_V, as key active sites for water decomposition, enhances the adsorption and dissociation of water molecules and promotes the formation of reaction intermediates. As shown in Fig. S23 (Supporting information), the ΔG for the initial water dissociation step ($H_2O \rightarrow OH^* + H^+ + e^-$) on β-PbO_2 (110) and (101) crystal faces with O_V are significantly reduced, with $\Delta G < 0$, indicating a favorable reaction energetics. In contrast, pristine β-PbO_2 (110) and (101) crystal planes exhibit higher ΔG and lower catalytic activity. These results demonstrate that designing porous structures to optimize the distribution of O_V is an effective strategy for improving O_3 generation performance.

In summary, we fabricated a 3D-porous β-PbO_2 anode on a Ti mesh substrate utilizing SiO_2 sphere template in conjunction with anodic deposition technique. Benefiting from the 3D interconnected porous architecture, the performance of electrochemical O_3 generation has been substantially enhanced. The FE for O_3 production by the 3D-porous β-PbO_2@Ti mesh anode reaches 14.73 %

at a current density of 100 mA/cm^2, markedly surpassing the performance of traditional β-PbO_2@Ti mesh anodes (6.11 %). Furthermore, this anode exhibits remarkable electrochemical stability, maintaining consistent O_3 production over 70 h at 100 mA/cm^2 and demonstrating sustained operation beyond 20 h even under the rigorous condition of 250 mA/cm^2. This advancement in O_3 generation and anode stability is attributed to the 3D structure of the anode, which optimizes external void configuration and Pb-O coordination environment, augmenting active sites for the electrocatalytic process. Consequently, this study not only presents a promising anode material for O_3 generation but also illustrates a promising strategy for modulating the intrinsic electrochemical properties of anodes *via* external structural design.

Declaration of competing interest

The authors declare that they have no known competing financial interests or personal relationships that could have appeared to influence the work reported in this paper.

CRediT authorship contribution statement

Mengqing Hu: Writing – review & editing, Writing – original draft, Validation, Software, Investigation, Data curation. **Di Zhao:** Writing – review & editing, Writing – original draft, Software, Methodology, Data curation. **Yun Wang:** Supervision, Conceptualization. **Jian Kang:** Software. **Ming Zhou:** Writing – review & editing, Data curation. **Huai Qin Fu:** Investigation, Formal analysis. **Bernt Johannessen:** Investigation. **Joshua Harbort:** Investigation. **Jeffrey Harmer:** Investigation. **Xinlong Yan:** Writing – review & editing. **Yajie Shu:** Writing – review & editing. **Porun Liu:** Writing – review & editing, Supervision, Methodology, Funding acquisition. **Huajie Yin:** Supervision, Funding acquisition, Conceptualization. **Huijun Zhao:** Supervision, Methodology, Funding acquisition, Conceptualization.

Acknowledgments

The authors thank the financial support from the National Natural Science Foundation of China (Nos. 52102197, 52102325), the Collaborative Innovation Program of Hefei Science Center, CAS (No. 2022HSC–CIP016), Australian Research Council (Nos. DP200100965, DP210104010, DP230102504). This research was undertaken in part on the XAS beamline at the Australian Synchrotron, part of ANSTO.

Supplementary materials

Supplementary material associated with this article can be found, in the online version, at doi:10.1016/j.cclet.2025.111192.

References

[1] C.V. Rekhate, J. Srivastava, Chem. Eng. J. Adv. 3 (2020) 100031.
[2] F. Yang, D. Wang, X. Zhang, et al., Chin. Chem. Lett. 35 (2024) 109599.
[3] S. Elodie, P. Gadonna-Widehem, T. Aussenac, Foods 10 (2021) 605.
[4] J. Chen, J.H. Davidson, Plasma Chem. Plasma Process. 22 (2002) 495–522.
[5] D.V. Franco, W.F. Jardim, J.F. Boodts, et al., Clean–Soil, Air, Water 36 (2008) 34–44.
[6] L.M.d. Silva, M.H. Santana, J.F. Boodts, Quim. Nova 26 (2003) 880–888.
[7] L.G. De Sousa, D.V. Franco, L.M. Da Silva, J. Environ. Chem. Eng. 4 (2016) 418–427.
[8] M. Rodríguez-Peña, J.A.B. Pérez, J. Llanos, et al., Curr. Opin. Electrochem. 27 (2021) 100697.
[9] Y. Gu, S. Wang, H. Shi, et al., ACS Catal. 11 (2021) 5438–5451.
[10] A.R. Rahmani, G. Azarian, D. Nematollahi, J. Electroanal. Chem. 824 (2018) 216–225.
[11] T. Watanabe, Y. Honda, K. Kanda, et al., Phys. Status Solidi 211 (2014) 2709–2717.
[12] Y. He, H. Lin, Z. Guo, et al., Sep. Purif. Technol. 212 (2019) 802–821.
[13] O. Shmychkova, V. Knysh, T. Luk'yanenko, et al., Surf. Eng. Appl. Electrochem. 54 (2018) 38–46.
[14] X. Wang, L. Wang, D. Wu, et al., Sci. Total Environ. 855 (2023) 158880.
[15] H. Guo, W. Hu, Z. Xu, et al., Process Saf. Environ. Prot. 164 (2022) 189–207.
[16] Y. Yao, X. Chen, N. Yu, et al., Russ. J. Electrochem. 54 (2018) 585–591.
[17] Y. Yao, X. Chen, N. Yu, et al., J. Electrochem. Soc. 164 (2017) E48.
[18] Q. Hu, Q. Yu, Z. Chen, et al., Int. J. Electrochem. Sci. 16 (2021) 1507124.
[19] S. Chai, G. Zhao, Y. Wang, et al., Appl. Catal. B: Environ. 147 (2014) 275–286.
[20] M. Hu, X. Yan, X. Hu, et al., J. Colloid Interface Sci. 510 (2018) 111–117.
[21] T. Sun, N. Shan, L. Xu, et al., Chem. Mater. 30 (2018) 1617–1624.
[22] Y. He, C. Qu, N. Ren, et al., Chin. Chem. Lett. 35 (2024) 109262.
[23] L. Huang, D. Li, J. Liu, et al., Environ. Sci. Pollut. Res. 27 (2020) 42072–42081.
[24] Z.J. Zhang, Q.Y. Zeng, S.L. Chou, et al., Electrochim. Acta 133 (2014) 570–577.
[25] X. Li, Y. Li, H. Zhang, et al., Chin. Chem. Lett. 32 (2021) 3221–3225.
[26] X. Wang, J. Wang, X. Tong, et al., Mater. Today Phys. 35 (2023) 101068.
[27] L. Burgio, R.J. Clark, S. Firth, Analyst 126 (2001) 222–227.
[28] I. Costantini, P.P. Lottici, K. Castro, et al., Minerals 10 (2020) 468.
[29] W. Hao, X. Chen, S. Li, J. Phys. Chem. C 120 (2016) 28448–28455.
[30] X. Wang, D. Wu, L. Wang, et al., J. Electrochem. Soc. 169 (2022) 106503.
[31] Q. Yu, X. Hu, ChemElectroChem 9 (2022) e202200919.
[32] W. Jiang, S. Wang, J. Liu, et al., J. Mater. Chem. A 9 (2021) 9010–9017.
[33] X. Wang, D. Wu, H. Ge, et al., J. Environ. Chem. Eng. 11 (2023) 110248.
[34] J. Liu, S. Wang, Z. Yang, et al., EES Catal. 1 (2023) 301–311.
[35] S.S. Jeon, P.W. Kang, M. Klingenhof, et al., ACS Catal. 13 (2023) 1186–1196.
[36] S.J. Li, Y. Lin, Z. Chen, et al., Chin. Chem. Lett. 21 (2010) 959–962.
[37] B. Wang, W. Wang, K. Sun, et al., Nano Res. 16 (2023) 11992–12012.
[38] Z. Zhang, Y. Li, L. Dong, et al., Chin. Chem. Lett. 34 (2023) 107404.
[39] C. Zhang, Y. Xu, P. Lu, et al., J. Am. Chem. Soc. 139 (2017) 16620–16629.
[40] G. Gibson, A. Morgan, P. Hu, et al., Chem. Phys. Lett. 654 (2016) 46–51.
[41] J.T. Jiang, Z. Guo, S.K. Deng, et al., ChemSusChem 17 (2024) e202400827.
[42] Y. Wang, M. Wang, Y. Yang, et al., Chem Catal. 3 (2023) 100643.
[43] Z. Song, Y. Jiang, Q. Gou, et al., Chin. Chem. Lett. 36 (2025) 109793.